Article:

Independent Control of Mode Selection and Power Extraction in Terahertz Semiconductor Lasers

Kai Wang[1,2], Hongzhou Bai[2,3], Chenren Yu[2,3], Haiqing Zhu[2,3], Pingping Chen[4], Wei Lu[4], Lianhe Li[5], A.Giles Davies[5], Edmund H. Linfield[5], Hua Li[6], Juncheng Cao[6], Chong Chen[7], Harvey E. Beere[7], David A. Ritchie[7] , Li He[2], Gangyi Xu[1,2,*]

1) Hangzhou Institute for Advanced Study, University of Chinese Academy of Sciences, Hangzhou 310024, China. 2) Key Laboratory of Infrared Imaging Materials and Detectors, Shanghai Institute of Technical Physics, Chinese Academy of Sciences, Shanghai 200083, China. 3) University of Chinese Academy of Sciences, Beijing 100049, China. 4) National Laboratory of Infrared Physics, Shanghai Institute of Technical Physics, Chinese Academy of Sciences, Shanghai 200083, China. 5) School of Electronic and Electrical Engineering, University of Leeds, Leeds LS2 9JT, UK. 6) Key Laboratory of Terahertz Solid State Technology, Shanghai Institute of Microsystem and Information Technology, Chinese Academy of Sciences, Shanghai 200050, China. 7) Cavendish Laboratory, University of Cambridge, Cambridge CB3 0HE, UK.

ABSTRACT: Mode selection and power extraction are the core of single-mode semiconductor lasers, but generally they restrict each other. A large gain area with high radiation efficiency is necessary for high output power but will induce more competitive modes and increase the threshold gain of the desired mode. Here, we demonstrate a novel laser cavity – an active distributed Bragg reflector (ADBR) and a grating coupler (GC) are monolithically integrated into a laser ridge – enabling independent control of mode selection and power extraction. The ADBR features a reflection peak with an extremely narrow bandwidth which releases the constraint on the cavity length, while the GC provides a controllable high radiation efficiency. The concept is implemented onto terahertz quantum cascade lasers, exhibiting robust single-mode emission with high output power and high operating temperature. Given the universality of the ADBR and GC, our concept can be utilized in different material systems at different wavelengths.

KEYWORDS: Quantum cascade laser, Terahertz, Active distributed Bragg reflector, Grating, Single mode, Photonic crystals, Monolithic integration.

High power single-mode semiconductor lasers are highly desired in numerous applications, ranging from high-precision spectral analysis, high speed communications, real-time imaging to biological diagnosis. To realize single-mode emission, distributed feedback and coupled-cavity are usually implemented in the compact semiconductor lasers[1]. The former can further be catalogued into 1D distributed feedback (DFB) lasers[2-5], 2D photonic crystal laser[6-7], distributed Bragg reflector (DBR) lasers[8] and vertical cavity surface emitting lasers (VCSEL)[9-11]. Although numerous efforts have been devoted to improving the stabilization of single-mode emission and the output power, in most of the cases, these two characteristics restrict each other. High output power demands a large gain area (i.e., laser cavity) and a high power efficiency. However, a large gain area induces more competitive laser modes in the cavity, while a high power efficiency indicates a high radiation loss of the desired mode. Both factors make the mode competition more complicated and deteriorate the stable operation of the desired mode.

Up to now, few kinds of laser cavities have been successfully proposed to simultaneously realize stable single-mode emission with an enlarged gain area and a high power efficiency. For the DFB lasers, strategies such as distributed feedback grating with central phase shift[12], chirped grating[13], graded photonic heterostructure[14], and hybrid Bragg grating[15] have been developed to improve the light emission efficiency. But the common difficulty is the limitation on the dimensions of the cavity for the reason to exclude the high-order longitudinal and transverse modes. For the DBR lasers, different kinds of DBR gratings such as high-order grating[16, 17] and sampled grating[18, 19] have been demonstrated to narrow the bandwidth of high reflectivity. However, the length of the active region section is still restricted to a few hundreds of micrometers to make the free spectral range larger than the reflectivity bandwidth. For VCSELs, in the short cavity between the DBR mirrors, the thin active region should spatially overlap with the intensity peak of the fundamental mode to enhance the discrimination against the adjacent longitudinal modes. Also, for the coupled-cavity lasers[20, 21], the primary cavity should be short to enhance the mode discrimination and to avoid mode hopping.

Notably, in the terahertz (THz) frequency range, the merging between the photonic and electronic concepts aroused a variety of novel cavity designs for high power single-mode terahertz quantum cascade lasers (THz-QCLs)[22-35]. For example, the third-order distributed feedback THz-QCLs were proven to be promising for low-divergence beam emission and high power efficiency[31]. Biasco et al. demonstrated continuous-wave highly-efficient low-divergence terahertz wire lasers[32]. Schönhuber et al. realized collimated laser beam via a random laser cavity[33]. Kao et al. developed phase-locked laser arrays through global antenna mutual coupling and realized single-mode THz-QCLs with a high slope efficiency and a nearly diffraction-limited beam divergence[25]. Similarly, Jin et al. demonstrated short-cavity laser arrays and, by phasing the radiative components,

realized an output power of 2.03 W and a slope efficiency of 1566 mW/A in pulsed mode[26]. Alternatively, by integrating microstrip antennas and micro reflectors in the third-order DFB grating, Khalatpour et al. demonstrated unidirectional lasers with a high wall-plug efficiency[27]. Furthermore, by exploiting π coupling, they realized phased arrays of THz photonic wire lasers with a continuous wave output of ~ 90 mW at cryogenic temperature[28]. Recently, Curwen et al. realized quantum-cascade metasurface-based vertical-external-cavity surface-emitting lasers (VECSEL) which exhibited broadband frequency tuning with a collimated beam and a high output power[29, 30]. Nevertheless, in each of these cavities, basically there is only one optical component that simultaneously controls the mode selection and the power extraction.

In this work, we demonstrate a novel cavity architecture to independently control the mode selection and the power extraction of a compact semiconductor laser (i.e., without an external mirror). The concept is implemented onto terahertz quantum cascade lasers (THz-QCLs). In our device an active distributed Bragg reflector (ADBR), a straight ridge (SR), and a grating coupler (GC) are monolithically integrated. When a distributed Bragg reflector (DBR) is loaded with appropriate gain – a so called ADBR – it enables an extremely narrow reflection peak at each photonic band-edge. Such a unique character will greatly release the constraint on the cavity length of a DBR laser. On the other hand, it has been proved that a GC can extract THz wave from a laser cavity with controllable radiation efficiency, low beam divergence, and nearly unidirectional emission[36]. Here, by monolithically integrating the ADBR and the GC into a laser ridge, we have demonstrated THz-QCLs exhibiting stable single-mode emission, large laser dimensions, and high power efficiency. The output power achieved in this work is comparable to the state-of-the-art ever reported in pulsed mode[26, 29]. The simplicity of the fabrication and the integrated structure make the mass productions and portable applications possible.

Results

Concepts. Figure 1(a) shows the schematic illustration of our proof-of-concept device, which is conceived to independently control the mode selection and power extraction via two individual photonic components. The device is based on a metal-metal waveguide, where the active region is sandwiched between the top and bottom metallic layers. The device consists of three functional sections: an active distributed Bragg reflector (ADBR), a straight ridge (SR) and a grating coupler (GC), and all share the same active region. In the ADBR section, a square lattice photonic crystal (PhC) – containing 2D periodic air holes in the top metallization – is formed near the left etched facet of the laser. The GC comprises 1D periodic air slits in the top metallization close to the right cleaved facet. Absorbing boundaries, which are composed by the high-loss n[+] GaAs top contact layer uncovered by the top metallization, are set between the ADBR and the left facet, and along the lateral sides of the ridge. The role of the absorbing boundaries is to perfectly

absorb the THz wave transmitting through the ADBR, as well as to eliminate the high order transverse modes, which are explained in detail in the Supplementary Note 1.

The role of the ADBR is to guarantee stable single-mode emission in a long cavity. Depending on the bias applied on the active region, a DBR can be passive or active and its reflectivity spectrum is qualitatively different. Considering an exemplar THz-QCL whose material gain peaks at ~2.9 THz, Figure 1(b) plots the calculated reflectivity spectra of a DBR when it is unbiased (corresponding to a waveguide loss of $\alpha \approx 17$ cm[-1]) or biased to different levels of net waveguide gain (g, the gain generated by the active region minus the waveguide loss). The calculations were carried out by 3D full-wave finite element method (FEM, see **Methods section**), and the structure parameters of the DBR are given in the caption of Fig. 1. Here, the key parameters are the radius of the air hole (r = 5μm) and the number of periods along the ridge direction (N_x = 40), which determines the Q-factor of the PhC. For the passive DBR (α=17 cm^{-1}), the reflectivity spectrum shows a plateau with a bandwidth of ~300 GHz which corresponds to the photonic band gap of the 2D PhC. In the case of g = 3.0 cm^{-1}, the reflectivity spectrum features two sharp peaks whose amplitudes exceed 1. The two reflectivity peaks orient from the field oscillation and amplification of the two band-edge modes, and their bandwidths decrease down to the order of 10 GHz. Note, only the low-frequency band-edge is of interest because the high-frequency one is far away from the peak of material gain. In the band-edge region, the phase of the reflected wave covers a range about π, as shown in the inset of Fig. 1(b), because the field oscillation inside the ADBR greatly increases the effective optical path. Figure 1(b) illustrates that the reflectivity of the ADBR is very sensitive to the net gain g, and when g increases from 3.0 cm^{-1} to 4.0 cm^{-1}, the peak reflectivity jumps from 1.6 to 5.7. The calculations strongly suggest that, with appropriate gain, the ADBR can operate as a perfect reflector that exhibits high reflectivity, extremely narrow bandwidth, and appropriate reflection phase. These features can be exploited to construct a single-mode laser with a long cavity.

The GC is utilized to efficiently extract electromagnetic (EM) wave out of the laser cavity, which is crucial for the THz frequency range where the high-quality anti-reflection coating is still lacking. Figure 1(c) plots the calculated reflectivity and the radiation efficiency of the GC as a function of frequency (g = 4 cm^{-1}), which indicate low reflectivity but high emission efficiency at the laser frequency f_0 (marked by the vertical dashed line which is determined by the ADBR). As we demonstrated in Ref. 36, the radiation efficiency of the GC can be flexibly controlled by the width of the air slit (W_{slit}) and the number of periods (N_{slit}). In addition, because of its large emission aperture and asymmetric location (i.e., close to the right facet), the GC enables nearly unidirectional radiation with low-divergence[36]. Consequently, a judicious combination of the ADBR and the GC will give rise to stable single-mode emission, high output power and low-divergence.
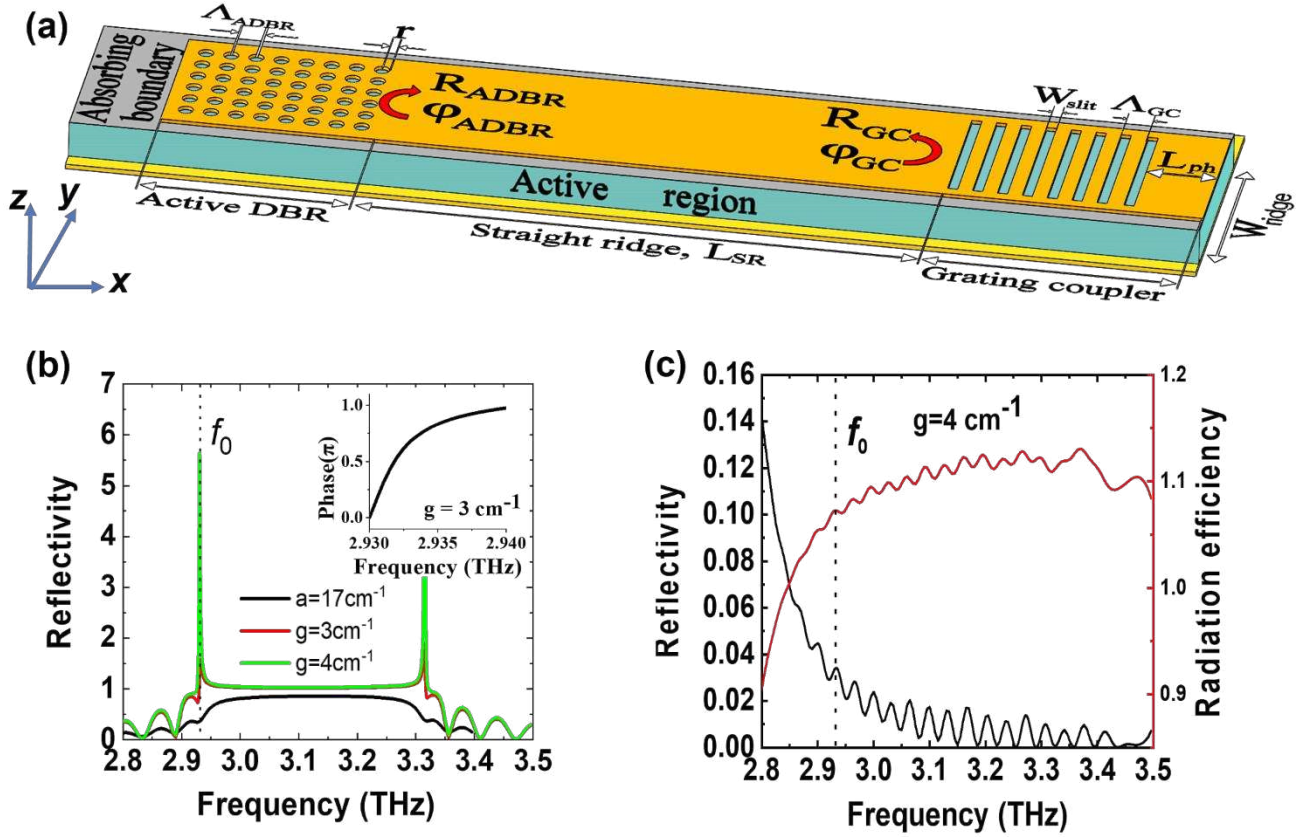
Figure 1 Concept of a THz semiconductor laser that independently controls the mode selection and power extraction. (a) Schematic illustration of the laser in which an active distributed Bragg reflector (ADBR), a straight ridge (SR) and a grating coupler (GC) are monolithically integrated in a metal-metal waveguide. For an exemplar THz-QCL with the material gain peaks at 2.9 THz, panel (b) plots the reflection spectra of the ADBR when g is respectively -17, 3.0 and 4.0 cm^{-1}. For the 2D PhC in the ADBR section, the periodicity (Λ_{ADBR}) is 13.9 μm, the hole radius (r) is 5.0 μm, and the number of periods (N_x) along the ridge is 40. Panel (c) plots the calculated spectra of reflectivity and radiation efficiency of the GC when g is 4.0 cm^{-1}. f_0 is the lasing frequency. For the GC section, the periodicity (Λ_{GC}) is 38 μm, the width of the air slit (W_{slit}) is 10 μm, and the number of the periods (N_{slit}) is 25.

Laser with an ADBR only. We firstly prove that a carefully designed ADBR can guarantee single-mode emission in a lengthened cavity. To this aim, we investigate a FP laser with an ADBR formed near the left facet, *i.e.*, a laser cavity similar to that shown in Fig. 1(a) but without the GC section. For simplicity, we term such laser as a THz-ADBR-QCL. Figures 2(a) and 2(b) show the schematic diagram and a typical SEM picture of the THz-ADBR-QCL. The intensity condition of the laser threshold reads

$$R_{ADBR} \times R_{facet} \times e^{2gL_{SR}} = 1 \qquad (1)$$

where R_{ADBR} is the frequency-dependent reflectivity of the ADBR which is closely related to its net loss or gain, R_{facet} the reflectivity of the cleaved facet, and L_{SR} the length of the straight ridge. The phase condition of the laser threshold reads:

$$\varphi_{ADBR} + 2n_{eff}k_0L_{SR} + \varphi_{facet} = 2m\pi \qquad (2)$$

where φ_{ADBR} is the frequency-dependent reflection phase of the ADBR, n_{eff} the effective refractive index, k_0 the wave vector in the free space, and φ_{facet} the reflection phase of the right cleaved facet, and m is an integer.

For the desired lasing frequency (~2.9 THz, close to the material gain peak), in our designed THz-ADBR-QCL, the ridge width (w_{ridge}) is 210 μm, L_{SR} is 2000 μm, the thickness of active region is 11.8 μm, and the absorbing boundary is 200 μm in length which is sufficiently long to absorb the THz wave transmitting through the ADBR. In the ADBR section, the variable parameters of the square lattice PhC include the periodicity (Λ_{ADBR}), the hole radius (r), the number of periods along the ridge (N_x). The number of periods perpendicular to the ridge is fixed as $N_y = 14$. Here, r and N_x determine the Q-factor of the 2D PhC and are the most critical parameters for the ADBR.

Here, we present the simulation results of an optimized THz-ADBR-QCL where Λ_{ADBR}, r and N_x are 13.9 μm, 5.0 μm and 40, respectively. In this structure, the modes whose frequencies locate in the photonic band gap of the ADBR reach the laser threshold first, because at low level of net gain the photonic band gap causes higher reflectivity than the bandedges. Figure 2(c) plots the accumulated intensity and phase – the left parts of Eq. (1) and Eq. (2) – of the THz wave after one round trip as a function of frequency when g is 1.0 cm^{-1}. At this gain level, there are several modes – whose frequencies locate in the photonic band gap of the ADBR – meeting the intensity and phase conditions of the laser threshold. Also because of the photonic band gap, for these modes, the EM field penetrated into the ADBR is negligible, as shown in Fig. 2(d) which presents the intensity

distribution ($|E_z|^2$) in the ADBR for one laser mode (f = 2.960 THz). Because of the spatial hole burning effect, beyond the threshold and with the increase of the injected current, the net gain in the ADBR (g_{ADBR}) will not be clamped at the level of 1.0 cm^{-1}. When g_{ADBR} increases up to 3.0 cm^{-1}, as shown in Figure 2(e), the accumulated round-trip intensity in the frequency range marked by the grey zone – which corresponds to the band-edge of the ADBR – is obviously higher
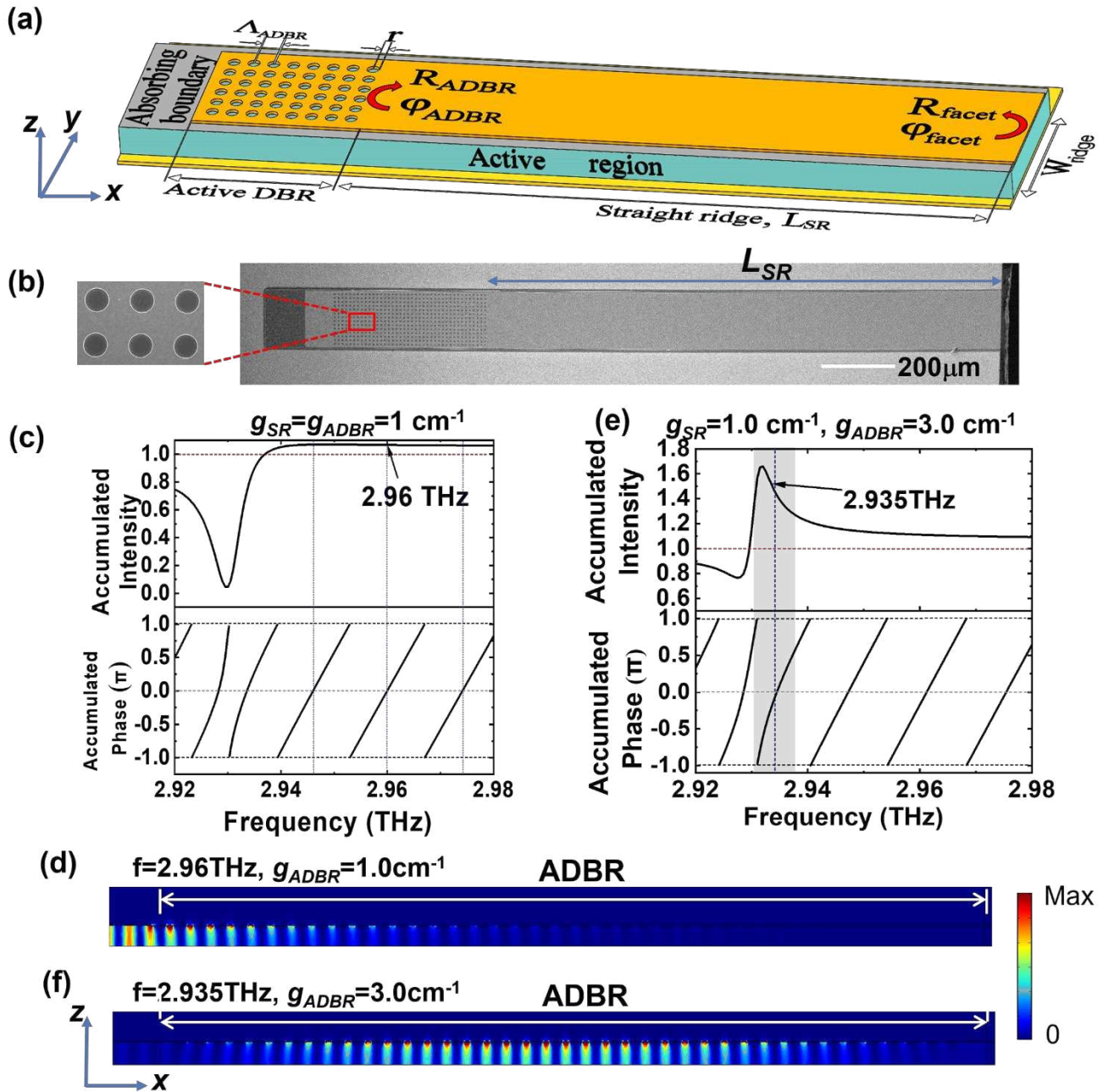

Figure 2 Operation principle of a THz-ADBR-QCL device. Panels (a) and (b) show the schematic diagram and the SEM picture of a typical THz-ADBR-QCL device. Panel (c) presents the accumulated intensity and phase of the EM wave after a round trip at different frequencies, where g_{SR} = g_{ADBR} = 1.0 cm^{-1}, and the modes located in the photonic band gap reach the threshold conditions. For one of these modes (f=2.960 THz), panel (d) gives the intensity ($|E_z|^2$) profile in the cross section (x-z plane) of the ADBR. Panel (e) plots the accumulated intensity and phase of the EM field at different frequencies, where g_{SR} = 1.0 cm^{-1} and g_{ADBR} = 3.0 cm^{-1}. The mode (f=2.935 THz) near the photonic band-edge meets the phase condition and its accumulated intensity exceeds 1, dominating the mode competition. Panel (f) shows the intensity ($|E_z|^2$) distribution in the ADBR for the mode f=2.935 THz. Note the field distributions in Panels (d) and (f) are respectively normalized and are not in the same scale.

than that in the photonic band gap. The reason is that, near the band-edge, the incident EM field will be oscillated, amplified and reflected back into the straight ridge, as shown in Fig. 2(f). Figure 2(e) also indicates that, in the frequency range marked by the grey zone, the accumulated phase covers nearly 2π. It means, regardless the uncertainty of the cavity length, there is always one mode in the band-edge region that meets the phase condition, and its accumulated intensity is evidently higher than those in the photonic band gap. As a result, the mode competition tends to force the

device operate on the mode whose frequency is in the band-edge of the ADBR. It is worth noting that the ADBR should not be regarded as a seed laser, since its threshold net gain is calculated to be 8.2 cm^{-1}, mainly due to the absorbing boundaries.

The reflection characteristic of the ADBR is closely related to its Q-factor. When N_x increases to 60, the Q-factor of the ADBR increases and the reflectivity peak appears with lower net gain. It makes the mode located at the band-edge reach the laser threshold first. However, when N_x decreases to 20, the Q-factor of the ADBR becomes so low that the reflection peak will not appear even when the net gain is as high as 6 cm^{-1}. It suggests that an ADBR with low Q-factor is not capable of mode selection. For the cases of N_x = 60 and N_x = 20, the calculated spectra of reflectivity and reflection phase at different waveguide loss or gain are shown in Figures S3 and S5 in Supplementary Note 2. The influences of Q-factor of the ADBR on the mode selection are also detailed in Supplementary Note 2.

Experimentally, the active region utilized in this work (wafer M1616) is based on a bound-to-continuum design[37], and the material gain covers the frequency range of 2.4-3.2 THz and peaks near 2.9 THz. THz-ADBR-QCLs with different N_x, Λ_{ADBR} and L_{SR} have been systematically fabricated and measured. For all the devices, the values of N_y, r and w_{ridge} are respectively 14, 5.0 μm and 210 μm. Details of the active region, device fabrication, and measurements are described in the **Methods section**.

We first studied the influence of the Q-factor of the ADBR on the device performance. To this aim, we compared three devices with the same Λ_{ADBR} (13.9 μm) and L_{SR} (2000 μm), but different N_x (20, 40, and 60). Figures 3 (a) – 3 (c) present the laser spectra of these devices measured at different bias conditions at a heat-sink temperature of 20 K. The device with low Q-factor (N_x = 20, Q = 55) operates on multimode whose frequencies locate in the band gap of the ADBR, as shown in Fig. 3 (a). In contrast, Figs. 3(b) and 3(c) illustrate that, devices with high Q-factor (N_x = 40, Q = 270 or N_x = 60, Q = 464) operate in single-mode and the side mode suppression ratio (SMSR) exceeds 22 dB during the whole dynamic range. More importantly, the emission frequency of the single mode locates exactly in the band-edge region, which strongly suggests that the ADBR provides a very narrow reflection peak resulting in single-mode emission. It is worth noting that, multimode emission was not observed for the devices N_x = 40 or 60, even when the injected current was just above the threshold. It is reasonable for the device with N_x = 60, since the simulations indicate that the mode located in the band-edge region reaches the threshold first. For the device with N_x = 40, the reason could be that the necessary net gain (g_{ADBR}) for the ADBR to activate single-mode emission (3.0 cm^{-1}) is close to the threshold net gain (1.0 cm^{-1}), as shown in Fig. 2.

Figure 3(d) illustrates the light-current-voltage (L-I-V) curves of the optimized THz-ADBR-QCL device (which is the same device as that shown in Fig. 3(b), Λ_{ADBR} = 13.9 μm, N_x = 40, L_{SR} = 2000 μm), measured in pulsed mode at different heat-sink temperatures. The peak output power and the threshold current density are respectively 12.5 mW and 226 A/cm^2 at 20 K, and the maximum operating temperature is 132 K. In Supplementary Note 3, we experimentally

investigated a reference THz-ADBR-QCL. The only difference between the optimized and the reference devices is that, in the latter there is a 3-μm-wide air gap in the top metallization between the ADBR and the straight ridge. Therefore, in the reference device the ADBR and the straight ridge can be biased simultaneously or separately. When only the ADBR is biased, the related threshold is 355 A/cm^2, much higher than the threshold (233 A/cm^2) when the whole device is simultaneously biased. It confirms that the ADBR acts as a narrowband reflector instead of a seed laser. Then, we fixed the current density of the SR at the level of maximum output (J_{SR} = 420 A/cm^2) and measured the emission spectra when the current density of the ADBR (J_{ADBR}) increased from 0 to 420 A/cm^2. When J_{ADBR} is below the threshold (233 A/cm^2), the device operates in multimode whose frequencies locate in the band gap of the ADBR. In contrast, when J_{ADBR} is above the threshold, the device operates in single mode whose frequency corresponds to the band-edge of the ADBR. The results unambiguously suggest that the gain in the ADBR (g_{ADBR}) is not clamped by the band gap modes, but increases with the injected current until the narrow reflection peak appears and forces the device to operate on the band-edge mode. The detailed experiment results are given in Supplementary Note 3.

To further investigate the mechanism of single-mode emission, we measured the emission spectra of 7 devices with the same N_x (N_x = 40), but different Λ_{ADBR} and L_{SR}. The results are presented in Fig. 3(e), in which the solid and dashed curves refer to the devices whose L_{SR} are 2000 μm and 2820 μm, respectively. Importantly, the emission wavelength changes approximately linearly with Λ_{ADBR}, which indicates that the emission wavelength is determined by the photonic band-edge of the ADBR.

It is worth emphasizing that, compared to the lasers with passive DBR[16-19], the cavity length of the lasers with the ADBR increases by approximately one order of magnitude. Recently Bismuto et al. experimentally demonstrated that, in a mid-infrared QCL containing a DBR and a FP section which were simultaneously biased, single-mode lasing can be realized even when the FP section is 5.25 mm in length[38]. However, in that paper, the mechanism of mode competition was not explained in detail.

Laser monolithically integrated with the ADBR and the GC. We then consider the whole structure where the ADBR and the GC are integrated on the two sides of the laser ridge, as schematically shown in Fig. 1(a). For simplicity, we term it a THz-ADBR-GC-QCL. The threshold conditions of the device become:

$$R_{ADBR} \times R_{GC} \times e^{2gL_{SR}} = 1 \qquad (3)$$

$$\varphi_{ADBR} + \varphi_{GC} + 2n_{eff}k_0L_{SR} = 2m\pi \qquad (4)$$

Here, R_{ADBR} (R_{GC}) and φ_{ADBR} (φ_{GC}) are the reflectivity and the reflection phase caused by the ADBR (GC) section, all of them are frequency-dependent. Figure 4 explains how the threshold conditions are satisfied in an optimized THz-ADBR-GC-QCL, in which the net gain of the waveguide is uniformly set as 4.0 cm^{-1}. The GC is designed to exhibit a radiation loss (α_{GC}) of ∼ 50 cm^{-1}, which is a tradeoff between the radiation efficiency and the laser dynamic range. Here, α_{GC} describes the decay of the EM field caused by the THz wave radiation when it propagates along the GC, and the
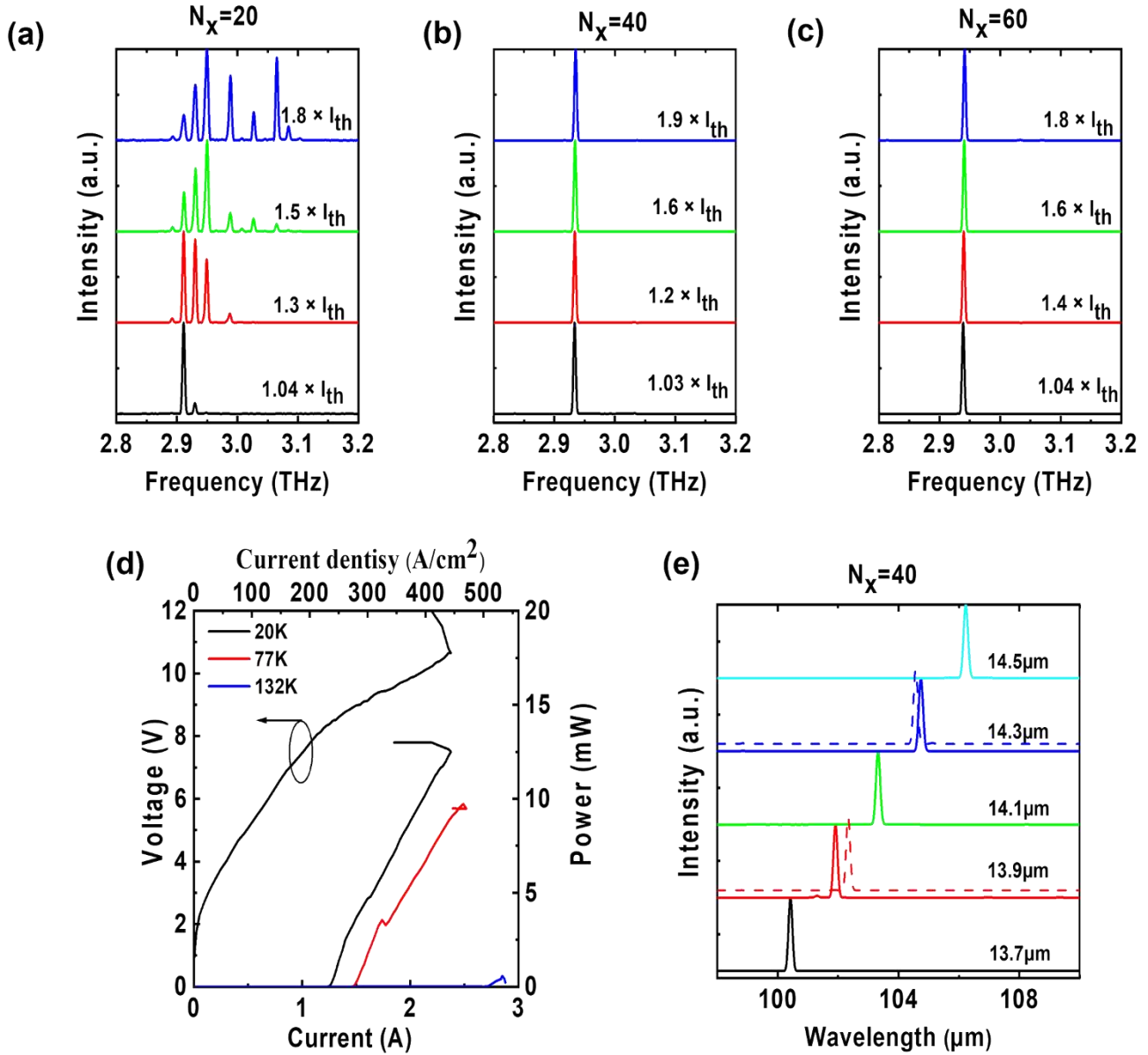
Figure 3 Spectral and light-current-voltage (*L-I-V*) characteristics of THz-ADBR-QCL devices. Panels (a) – (c) show the normalized laser spectra of 3 devices measured at 20K with different injected currents. I_{th} refers to the threshold current. The devices have the same L_{SR} (2000 µm) and Λ_{ADBR} (13.9 µm), and the only varied parameter is N_x, which is 20 (a), 40 (b), and 60 (c). The value of N_x and the injected currents are marked in each panel. Panel (d) plots the *L-I-V* curves measured in pulsed mode at different operating temperatures for an optimized device (the same device as that shown in panel (b), L_{SR}=2000 µm, Λ_{ADBR} =13.9 µm, N_x = 40, r = 5.0 µm). Panel (e) shows the normalized laser spectra of a group of devices in which N_x = 40, and Λ_{ADBR} changes from 13.7 µm to 14.5 µm. The solid (dashed) curves correspond to the devices where L_{SR} equals to 2000 µm (2820 µm). The laser spectra are shifted vertically for clarity, and the values of Λ_{ADBR} are marked. All the spectra are measured at the bias condition of peak output and at a heat-sink temperature of 20K.

deduction of α_{GC} is detailed in Supplementary Note 4. The details of structure parameters are given in the caption of Fig. 4. Figures 4(a) and 4(b) show the calculated reflectivity spectra of the GC and the ADBR, respectively. In the frequency range of interest, the reflectivity of GC (R_{GC}) oscillates slightly around 0.02. The low value of R_{GC} is caused by the high radiation loss (50 cm⁻¹) of the GC. The oscillation of R_{GC} is due to the resonator feature of the GC, as well as the interference between the GC and the cleaved right facet. Figures 4(c) and 4(d) respectively present the calculated accumulated intensity and phase after a round trip. In the frequency range marked by the grey zone, the accumulated

intensity excesses one and the accumulated phase covers almost 2π. It suggests that during the increasement of the net gain g up to 4.0 cm⁻¹, there is only one mode in the band-edge region that satisfies the threshold conditions.
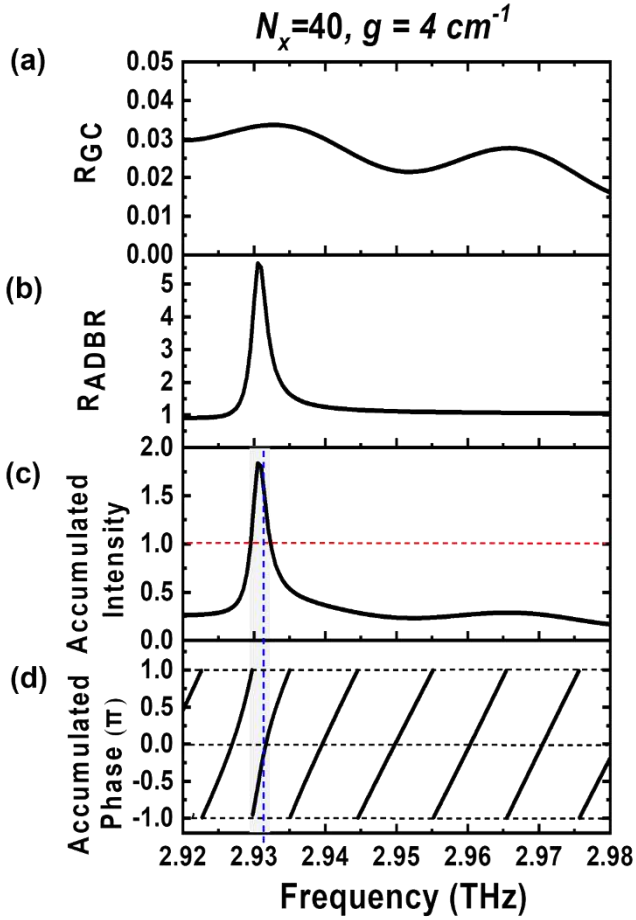
N_x=40, g = 4 cm^{-1}

(a)

(b)

(c)

(d)

Figure 4 Threshold conditions for an optimized THz-ADBR-GC-QCL. In the ADBR section, N_x= 40, N_y=14, r = 5.0 μm, Λ_{ADBR} =13.9 μm. In the SR section, L_{SR} = 3200 μm. In the GC section, Λ_{GC}= 38 μm, W_{slit}=10 μm, N_{slit}= 25. Panels (a) and (b) plot respectively the calculated reflectivity spectra of the GC and the ADBR. Panels (c) and (d) plot respectively the accumulated intensity and phase after a round trip. The net gain (g) of the waveguide is uniformly set as 4.0 cm^{-1}.

In order to validate our hypothesis, we fabricated and measured several groups of THz-ADBR-GC-QCLs. In each group, there are 4 devices that have the same structures of the ADBR and GC, and the same value of L_{SR}. The only difference is the distance (L_{ph}) between the GC and the right cleaved facet, and the interval between the values of L_{ph} is 3.5μm (defined by the technique of photolithography) which is approximately the eighth part of the effective wavelength in the waveguide. Therefore, for a fixed laser frequency, these 4 devices represent 4 different reflection phases caused by the grating coupler (φ_{GC}). Figures 5(a) – 5(c) show the measurement results of an exemplar group of devices. For these 4 devices, the common structure parameters are listed in Table 1, and the only varied parameter is L_{ph}, which varies from 311.2 μm to 321.7 μm. Figure 5(a) shows the SEM picture of the 4 devices. Figure 5(b) presents their light-current-voltage (*L-I-V*) curves measured at 20K in pulsed mode, revealing that the devices exhibit almost the same threshold current, and their peak output power reaches around 185 mW. Most importantly, Figure 5(c) presents the emission spectra of the 4 devices near the maximum output, demonstrating single-mode emission with

their laser frequencies locating exactly in the band-edge region. Figure S10 of Supplementary Note 5 presents the
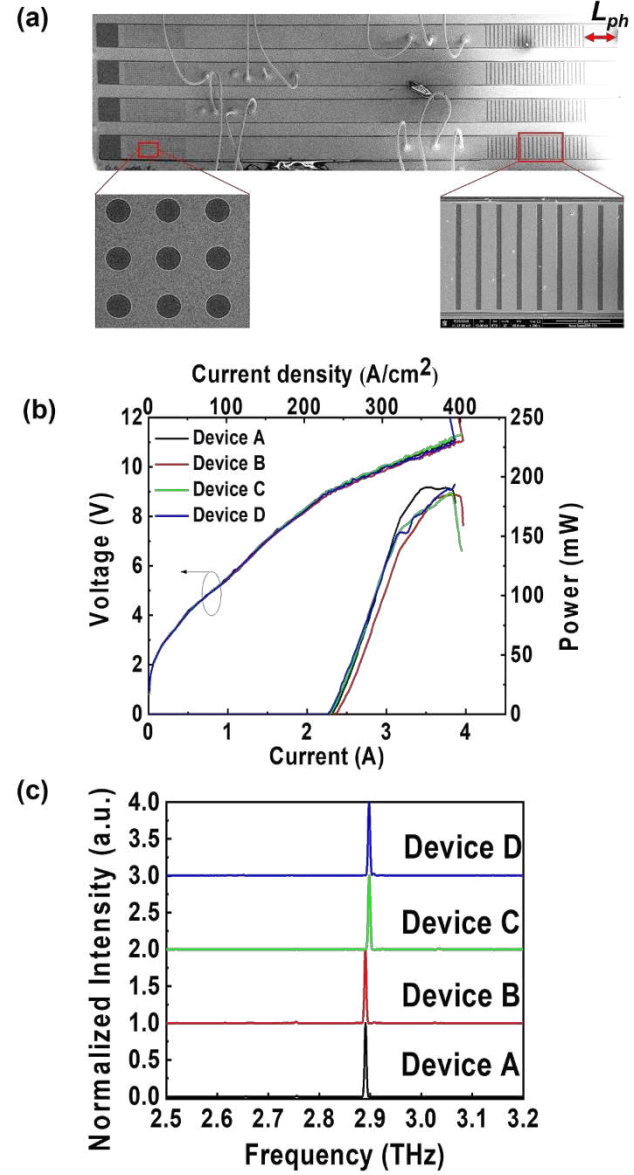

Figure 5 Influence of the cavity length on the performance of the THz-ADBR-GC-QCL devices. (a) SEM images of 4 THz-ADBR-GC-QCL devices, whose common structure parameters are listed in Table 1, and the only varied parameter is L_{ph}. The values of L_{ph} are 311.2, 314.7, 318.2, 321.7 μm for devices A, B, C and D, respectively. (b) *L-I-V* curves of the 4 devices. (c) Normalized spectra of the 4 devices at maximum output. The laser spectra are shifted vertically for clarity. The measurements were carried out at 20K in pulsed mode. The repeat frequency is 10 kHz, and the pulse length is 1 μs.

emission spectra at different injected currents for these devices, proving that single-mode emission was realized in most part of the laser dynamic range. The results reveal that, despite the uncertainty of the reflection phase φ_{GC}, the narrow reflection peak of the ADBR dominates the mode selection. The *L-I-V* curves of these 4 devices were also measured at different operating temperatures and the results are described in Supplementary Note 5.

Table1 Common structure parameters used in the exemplar group of THz-ADBR-GC-QCL devices.

Ridge width	Straight ridge section	ADBR section				GC section		
w_{ridge}	L_{SR}	Λ_{ADBR}	r	N_x	N_y	Λ_{GC}	W_{slit}	N_{slit}
210 μm	3200 μm	14.1 μm	5.0μm	40	14	38 μm	10 μm	25

In order to make our concept more solid, we measured another 4 THz-ADBR-GC-QCLs, where the only varied structure parameter is Λ_{ADBR} which varies from 13.7 μm to 14.3 μm. The emission spectra of these 4 devices are recorded in Fig. S11 of the Supplementary Note 6, illustrating that single-mode operation is achieved and the emission wavelength varies linearly with Λ_{ADBR}, confirming the robustness of the mode selection.

Figure 6 shows the laser characteristics of an optimized device, in which the laser frequency aligns with the material gain peak. Figure 6(a) illustrates *L-I-V* curves measured at different operating temperatures. The peak output power reaches to 214 mW at 20 K, and remains 168 mW at 77 K. The maximum operating temperature is 121 K. At 20 K, the threshold current density, the slope efficiency (*dP/dI*) and the wall-plug efficiency (*WPE*) are 228 A/cm^2, 188 mW/A and 0.54%, respectively. The normalized spectra of the device measured under different injected currents at 20 K are recorded in Fig. 6(b). Essentially, in the whole dynamic range, single-mode emission is realized, and the SMSR exceeds 25 dB under the bias of peak output. Figure 6(c) shows the measured 2D far-field beam pattern of the device, which features a single-lobed beam pattern and the FWHM divergence angle is ~8° × 33°. The definition of the scanning angles (θ_x and θ_y) during the measurement of beam pattern and the simulated beam pattern are given in Figure S12 in Supplementary Note 7. Good agreement between the simulation and the measurement confirms that the THz wave is emitted from the GC surface.

In order to exclude the influence of material quality and highlight the advantage of efficient power extraction in our THz-ADBR-GC-QCL devices, comparative experiments have been conducted. Multimode FP lasers with the semi-insulator single-plasmon (SISP) waveguide or metal-metal (MM) waveguide have been fabricated from the same material, and the device dimensions are respectively 295×3400 μm^2 and 210×3900 μm^2, similar to that of the THz-ADBR-GC-QCLs. The *L-I-V* curves of all three kinds of lasers were measured under the same conditions in pulsed mode at 20 K, and the typical results are shown in Figure 6(d). Table 2 lists the calculated and measured parameters for the optimized THz-ADBR-GC-QCL, the THz-ADBR-QCL, the FP-MM, and the FP-SISP laser. Compared with the FP-SISP multimode laser, the THz-ADBR-GC-QCL device doubles the peak output power and the wall plug efficiency. On the other hand, the output power and the wall plug efficiency of the THz-ADBR-GC-QCL device are approximately 20 times higher than those of the FP-MM laser. The maximum operation temperature of the THz-ADBR-GC-QCL (121 K) is in between those of the FP-MM laser (135 K) and the FP-SISP laser (105 K). The tendencies of measured results (J_{th}, P_{out}, *dP/dI*, *WPE*, T_{max}) for these 4 different devices are qualitatively consistent with their calculated parameters (Γ, α_{tot}, α_{rad}). In Supplementary Note 8, we propose an experimental approach to determine the reflectivity of the ADBR, and the related work is under way.

To make our concept more general, the THz-ADBR-GC-QCL devices were fabricated with a different material (wafer L1162) operating at different laser frequency (~3.3 THz). The results are given in Supplementary Note 9. For a typical device, the pulsed output power peaks at 366 mW at 20 K, and remains 224 mW at 77 K, comparable to the state-of-the-art[26, 29]. The related slope efficiency and the wall plug efficiency are respectively 152mW/A and 0.4% at 20K. The maximum operating temperature reaches to 147 K which is – to our best knowledge – the highest record ever reported for high power (>100 mW) single-mode THz-QCLs. Single-lobed beam pattern is obtained, and the divergence angle at FWHM is about 7°×34°. Stable single-mode operation is observed and the emission wavelength varies from 88.9 to 93.2 μm when Λ_{ADBR} changes from 12.0 to 12.6 μm. It is interesting to point out that, these THz-ADBR-GC-QCL devices have been utilized to detector H_2S gas track by means of photoacoustic spectroscopy, and a detection limit down to 360 ppb has been realized[39].

Discussion

By optimizing the structure design, it is available to further improve the laser performances. The reflectivity of the ADBR is highly sensitive to the Q-factor of the 2D PhC. By modifying the filling factor, utilizing elliptical air holes, and optimizing the periodicity and the number of periods along the lateral direction, we can increase the Q-factor of the 2D PhC and achieve more stable single-mode emission with lower threshold. Essentially, a 1D grating can also be used as the ADBR with even better effects. Firstly, a grating possesses a wider band gap, and therefore we can safely utilize one reflection peak by pushing the other far away from the material gain peak. Secondly, compared with the 2D PhC, by modifying the width of air slits, a grating can reach to the same Q-factor with less periods and therefore reduce the power consumption of the device.
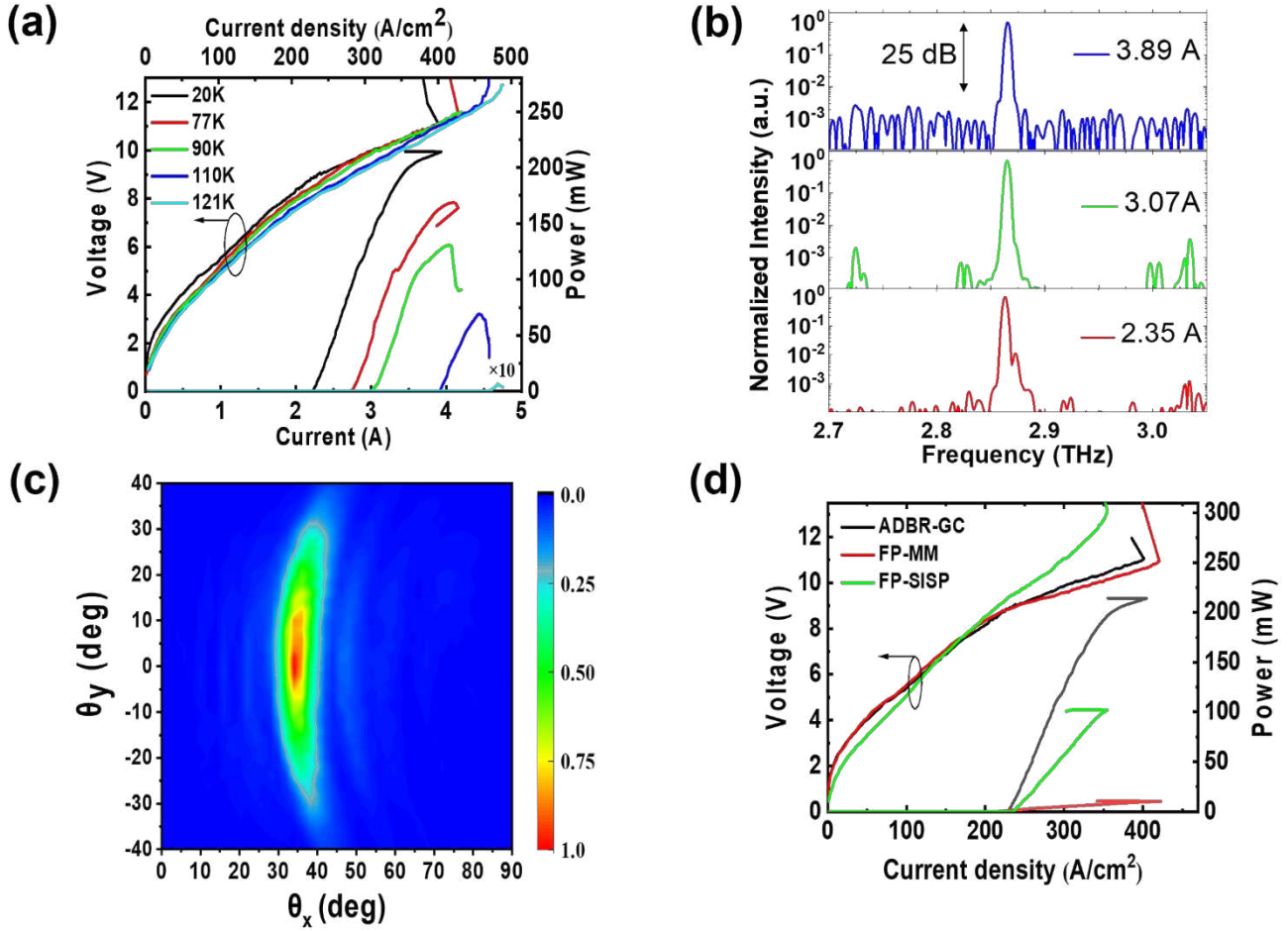
Figure 6 Device performances of an optimized THz-ADBR-GC-QCL (Panels (a) to (c)), and its comparison with the FP lasers from the same material (Panel (d)). The structure parameters are: Λ_{ADBR} = 14.3 μm, N_x = 40, r = 5.0 μm, Λ_{GC} = 38.0 μm, N_{slit} = 25, W_{slit} = 10.0 μm, L_{SR}=3200 μm. (a) L-I-V curves measured in pulsed mode at different operating temperatures. (b) Normalized emission spectra measured at different injected currents at 20K. (c) Far-field beam pattern measured at 20K. (d) Light-current density-voltage (L-J-V) curves of the optimized THz-ADBR-GC-QCL, the FP-MM laser and the FP-SISP laser measured at 20 K. All devices were fabricated with the same material.

Table 2 The calculated and the measured parameters of the optimized THz-ADBR-GC-QCL, the THz-ADBR-QCL, the FP-MM, and the FP-SISP lasers, all from the same material (M1616). Γ is the optical confinement factor, α_{tot} the total loss, α_{rad} the radiation loss, J_{th} the threshold current density, P_{out} the peak output power, dP/dI the slope efficiency, WPE the wall-plug-efficiency, T_{max} the maximum operating temperature.

	Calculations			Experiment results				
	Γ	α_{tot}	α_{rad}	Measured at 20K				T_{max}
		(cm⁻¹)	(cm⁻¹)	J_{th} (A/cm²)	P_{out} (mW)	dP/dI (mW/A)	WPE	(K)
THz-ADBR-GC-QCL	0.98	21	5.6	228	214	188	5.4×10^{-3}	121
THz-ADBR-QCL	0.98	20	0.6	226	12.5	11.5	5.0×10^{-4}	132
FP-MM	0.98	17.6	0.3 (per facet)	212	10.5	6.5	2.8×10^{-4}	135
FP-SISP	0.26	8.3	1.1 (per facet)	238	102	89	2.2×10^{-3}	105

The beam quality of the THz-ADBR-GC-QCL device can be further improved via optimizing the design of the GC. In a third-order DFB THz-QCL that features low beam divergence, the grating should satisfy the third-order Bragg condition and simultaneously act as an array of phased linear sources[31]. It leads to a rigorous requirement on the design of the grating, i.e., the effective index of the waveguide should be close to 3. In contrast, in our device the mode selection is controlled by the ADBR, and the GC is used to manipulate the power extraction and beam pattern. Such strategy makes the design of the GC more flexible, and essentially there is no constraint on the effective index of the waveguide. By tuning the periodicity of the GC and thus making k_x (wave vector along the ridge) of the -1-order diffraction – which corresponds to the extracted THz radiation – close to the wave vector in the free space, the GC will enable grazing-emission with low divergence. On the other hand, the radiation efficiency is mainly determined by N_{slit} and W_{slit} of the GC. Careful design is necessary to balance the radiation efficiency, the threshold, and the laser consumption.

To further improve the output power in pulsed mode, a wide ridge together with correctly designed lateral absorbing boundaries can be exploited to increase the dimension of the active region. Contrarily, a narrow ridge (≤ 40 μm) will significantly decrease the power consumption and improve the heat dissipation in the lateral directions, which is important for continuous-wave operation.

Conclusion

In conclusion, we realized a new cavity architecture to independently control the mode selection and power extraction in the THz-QCLs. In the demonstrated devices, the ADBR acts as a reflector with high reflectivity and extremely narrow bandwidth, which enables single-mode emission and releases the constraint on the cavity length. The GC permits controllably high radiation efficiency, nearly unidirectional emission and low divergence. The combination of ADBR and GC results in a high output power (224 mW) of single-mode operation at liquid nitrogen temperature in pulsed mode, which is comparable to the state-of-the-art. Essentially, there is no limit on the material system to build the ADBR and GC sections. Therefore, the concept can be exploited in a wide spectral range from near-infrared to terahertz frequency range.

Methods

Materials. Two different kinds of QCL active region were employed, both grown on a semi-insulator GaAs substrate via molecular beam epitaxy (MBE), and consisting of a GaAs/ $Al_{0.15}Ga_{0.85}As$ heterostructure and based on a bound-to-continuum active transition with one-well injector. The first structure (wafer M1616) is similar to the design reported in Ref. 37, with layer sequence: **5.5**/11.0/**1.8**/11.5/**3.8**/9.4/**4.2**/18.4 (in nm), where $Al_{0.15}Ga_{0.85}As$ layers are indicated in bold, and the underlined number corresponds to the layer with a Si doping concentration of 2×10^{16} cm^{-3}. The active region consists of 180 stages with a total thickness of 11.8 μm. The frequency range of the gain is approximately 2.4 – 3.2 THz, deduced from the results of the second-order DFB lasers. The second structure (wafer L1162) is the same as that in Ref. 40. The layer sequence of each repeated module in the active region is: **5.2**/10.3/**1.7**/10.75/**3.6**/8.8/**3.95**/17.2 (in nm), where

the Si-doped layer (3×10^{16} cm^{-3}) is underlined. The total thickness of the active region is 11.1 μm.

Fabrication. The processes of fabrication are the same as that described in Ref. 36. After epitaxy, the sample was bonded on an n$^+$ GaAs substrate with an Au-Au interface. The semi-insulator GaAs substrate was then removed via mechanical polishing followed by selective wet-etching. Once the GaAs/AlGaAs epitaxy was exposed, the top n$^+$ GaAs (600 nm in thickness) contact layer was partially removed by wet etching. After that, the absorbing boundaries were defined by photolithography. The top metallization was then formed on the top of the active region, defined by contact photolithography, e-beam evaporation, and lift-off. The grating coupler and the photonic crystal were also formed in this step via defining periodic air slits and holes on the top metallization. Later, the device ridge was defined by chlorine-based inductively coupled plasma (ICP) etching. Finally, the back-side process consisted of substrate thinning, Ti/Au evaporation and sample cutting via micro-dicing with a diamond blade.

Simulations. The characteristics of the ADBR and the GC – including the reflection and radiation spectra, the Q-factor, and the far-field beam emission pattern – were calculated by full-wave finite element method (FEM) with a commercial solver of COMSOL Multiphysics. The real part of the effective refraction index of the waveguide was set as $n_{eff} = 3.50$, and the waveguide loss caused by the free carrier absorption and the metallic Ohm loss was approximated as 17 cm^{-1}, computed by the Drude model. During the calculation of Q-factor of the DBR, the waveguide loss was not taken into consider, therefore the Q-factor corresponds to the leakage of the EM field out of the DBR. To simplify the calculation, the metallization layers are considered as perfect electric conductors, and the epilayers were considered as a uniform material with appropriate loss and gain. 2D and 3D FEM simulations were carried out for the GC and ADBR sections, respectively.

Measurement details. All the devices were measured in pulsed mode. The pulse width and the repeat frequency were respectively 1 μs and 10 kHz. The spectral characteristics were performed using a Fourier transform infrared spectrometer (Bruker 80V), operating in fast scan mode with a resolution of 0.1 cm^{-1}. The output power was measured by a Golay cell, which was put just in front of the TPX window of the cryostat and no cone was used, without any correction for the imperfect collection efficiency and optical loss from the cryostat window. The Golay cell was calibrated by a Thomas Keating absolute THz power meter. The far-field emission patterns of the devices were measured with the Golay cell detector, which was scanned on a 15-cm-radius sphere centered on the device surface. In our measurement setup, we used a 4-mm-thick TPX window whose transmission coefficient is about 60%. Considering the beam divergence, the collection efficiency for the THz-ADBR-GC-QCL was about 50%.

ASSOCIATED CONTENT

Supporting Information. "The Supporting Information is available free of charge via the Internet at http://pubs.acs.org."

AUTHOR INFORMATION

Corresponding Author

* email: gangyi.xu@mail.sitp.ac.cn.

Author Contributions

The manuscript was written through contributions of all authors.

REFERENCES

[1]   Coldren, L. A., Corzine, S. W. & Mashanovitch, M. L. Diode lasers and photonic integrated circuits. (John Wiley & Sons, Inc., **2012**, Hoboken).

[2]   Kazarinov, R. & Henry, C. Second-order distributed feedback lasers with mode selection provided by first-order radiation losses. *IEEE J. Quantum Electron.* **1985**, 21, 144-150.

[3]   Macomber, S. H.; Mott, J. S.; Noll, R. J.; Gallatin, G. M.; Gratrix, E. J.; O'Dwyer, S. L.; Lambert, S. A. Surface‐emitting distributed feedback semiconductor laser. *Appl. Phys. Lett.* **1987,** 51, 472-474.

[4]   Boyle, C.; Sigler, C.; Kirch, J. D.; Lindberg III, D. F.; Earles, T.; Botez, D.; Mawst, L. J. High-power, surface-emitting quantum cascade laser operating in a symmetric grating mode. *Appl. Phys. Lett.* **2016**, 108, 121107.

[5]   Kao, T. Y.; Hu, Q.; Reno, J. L. Phase-locked arrays of surface-emitting terahertz quantum-cascade lasers. *Appl. Phys. Lett.* **2010**, 96, 101106.

[6]   Painter, O.; Lee, R. K.; Scherer, A.; Yariv, A.; O'brien, J. D.; Dapkus, P. D.; Kim, I. Two-Dimensional Photonic Band-Gap Defect Mode Laser, *Science* **1999**, **284**, 1819.

[7]   Noda, S.; Yokoyama, M.; Imada, M.; Chutinan, A.; Mochizuki, M. Polarization Mode Control of Two-Dimensional Photonic Crystal Laser by Unit Cell Structure Design. *Science* **2001**, 293, 1123.

[8]   Arimoto, H.; Kitatani, T.; Tsuchiya, T.; Shinoda, K.; Takei, A.; Uchiyama, H.; Tsuji, S. Wavelength-tunable short-cavity DBR laser array with active distributed Bragg reflector. *J. Lightwave Technol.* **2006**, 24, 4366-4371.

[9]   Jager, R.; Grabherr, M.; Jung, C.; Michalzik, R.; Reiner, G.; Weigl, B.; Ebeling, K. J. 57% wallplug efficiency oxide-confined 850 nm wavelength GaAs VCSELs. *Electron. Lett.* **1997**, 33, 330-331.

[10]   Iga, K. Surface-emitting laser-its birth and generation of new optoelectronics field. *IEEE J. Sel. Top. Quantum Electron.* **2000**, 6, 1201-1215.

[11]   Siriani, D. F.; Choquette, K. D. Electronically controlled two-dimensional steering of in-phase coherently coupled vertical-cavity laser arrays. *IEEE Photonics Technol. Lett.* **2010**, 23, 167-169.

[12]   Li, S.; Witjaksono, G.; Macomber, S.; Botez, D. Analysis of surface-emitting second-order distributed feedback lasers with central grating phaseshift. *IEEE J. Sel. Top. Quantum Electron.* **2003**, 9, 1153-1165.

[13]   Xue, L.; Brueck, S.; Kaspi, R. Widely tunable distributed-feedback lasers with chirped gratings. *Appl. Phys. Lett.* **2009**, 94, 161102.

[14]   Xu, G.; Colombelli, R.; Khanna, S. P.; Belarouci, A.; Letartre, X.; Li, L.; Linfield, E. H.; Davies, A. G.; Beere, H. E.; Ritchie, D. A. Efficient power extraction in surface-emitting semiconductor lasers using graded photonic heterostructures. *Nat. Commun.* **2012**, 3, 1-7.

[15]   Jin, Y.; Gao, L.; Chen, J.; Wu, C.; Reno, J. L.; Kumar, S. High power surface emitting terahertz laser with hybrid second-and fourth-order Bragg gratings. *Nat. Commun.* **2018**, 9, 1-7.

[16]   Feise, D.; John, W.; Bugge, F.; Blume, G.; Hassoun, T.; Fricke, J.; Paschke, K.; Erbert, G. 96 mW longitudinal single mode red-emitting distributed Bragg reflector ridge waveguide laser with tenth order surface gratings. *Opt. Lett.* **2012**, 37, 1532-1534.

[17]   Abdullaev, A.; Lu, Q.; Guo, W.; Wallace, M. J.; Nawrocka, M.; Bello, F.; Benson, A.; O'Callaghan, J.; Donegan, J. F. Improved performance of tunable single-mode laser array based on high-order slotted surface grating. *Opt. Express* **2015**, 23, 12072-12078.

[18]   Coldren, L. A. Monolithic tunable diode lasers. *IEEE J. Sel. Top. Quantum Electron.* **2000**, 6, 988-999.

[19] Jayaraman, V.; Chuang, Z. M.; Coldren, L. A. Theory, design, and performance of extended tuning range semiconductor lasers with sampled gratings, *IEEE J. Quantum Electron.* **1993**, 29, 1824.

[20]   Fuchs, P.; Seufert, J.; Koeth, J.; Semmel, J.; Höfling, S.; Worschech, L.; Forchel, A. Widely tunable quantum cascade lasers with coupled cavities for gas detection. *Appl. Phys. Lett.* **2010**, 97, 181111.

[21]   Pierściński, K.; Pierścińska, D.; Pluska, M.; Gutowski, P.; Sankowska, I.; Karbownik, P.; Czerwinski, A.; Bugajski, M. Room temperature, single mode emission from two-section coupled cavity InGaAs/AlGaAs/GaAs quantum cascade laser. *J. Appl. Phys.* **2015**, 118, 133103.

[22]   Köhler, R.; Tredicucci, A.; Beltram, F.; Beere, H. E.; Linfield, E. H.; Davies, A. G.; Ritchie, D. A.; Iotti, R. C.; Rossi, F. Terahertz semiconductor-heterostructure laser, *Nature* **2002**, 417, 6885.

[23]   Williams, B. S. Terahertz quantum-cascade lasers. *Nat. Photonics* **2007**, 1, 517–525.

[24] Sirtori, C.; Barbieri, S.; Colombelli, R. Wave engineering with THz quantum cascade lasers. *Nat. Photonics* **2013**, 7, 691.

[25] Kao, T. Y.; Reno, J. L; Hu, Q. Phase-locked laser arrays through global antenna mutual coupling. *Nat. Photonics* **2016**, 10, 541-546.

[26]   Jin, Y.; Reno, J. L; Kumar, S. Phase-locked terahertz plasmonic laser array with 2W output power in a single spectral mode. *Optica* **2020**, 7, 708-715.

[27] Khalatpour, A.; Reno, J. L.; Kherani, N. P; Hu, Q. Unidirectional photonic wire laser, *Nat. Photonics* **2017**, 11, 555-559.

[28] Khalatpour, A.; Reno, J. L; Hu, Q. Phase-locked photonic wire lasers by π coupling. *Nat. Photonics* **2019**, 13, 47-53.

[29]   Curwen, C. A.; Reno, J. L; Williams, B. S. Terahertz quantum cascade VECSEL with watt-level output power. *Appl. Phys. Lett.* **2018**, 113, 011104.

[30]   Curwen, C. A.; Reno, J. L; Williams, B. S. Broadband continuous single-mode tuning of a short-cavity quantum-cascade VECSEL. *Nat. Photonics* **2019**, 13, 855-859.

[31] Amanti, M. I.; Fischer, M.; Scalari, G.; Beck, M; Faist, J. Low-divergence single-mode terahertz quantum cascade laser. *Nat. Photonics* **2009**, 3, 586–590.

[32] Biasco, S.; Garrasi, K.; Castellano, F.; Li, L.; Beere, H. E.; Ritchie, D. A.; Linfield, E. H.; Davies, A. G.; Vitiello, M. S. Continuous-wave highly-efficient low-divergence terahertz wire lasers. *Nat. Commun.* **2018**, 9, 1-8.

[33] Schonhuber, S.; Brandstetter, M.; Hisch, T.; Deutsch, C.; Krall, M.; Detz, H.; Andrews, A. M.; Strasser, G.; Rotter, S.; Unterrainer, K. Random lasers for broadband directional emission, *Optica* **2016**, 3, 1035.

[34] Xu, G.; Li, L.; Isac, N.; Halioua, Y.; Davies, A. G.; Linfield, E. H.; Colombelli, R. Surface-emitting terahertz quantum cascade lasers with continuous-wave power in the tens of milliwatt range, *Appl. Phys. Lett.* **2014**, 104, 091112.

[35] Zhu, H.; Zhu H.; Yu, C.; Chang, G.; Wang, F.; Chen, J.; Li L.; Davies, A. G.; Linfield, E. H.; Tang Z.; Chen, P.; Lu, W.; Xu, G.; He, L. Modeling and improving the output power of terahertz master-oscillator power-amplifier quantum cascade lasers, *Opt. Express* **2020**, 28, 23239.

[36] Yu, C.; Zhu, H.; Wang, F.; Chang, G.; Zhu, H.; Chen, J.; Chen, P.; Tang, Z.; Lu, W.; Shen, C. Highly efficient power extraction in terahertz quantum cascade laser via a grating coupler. *Appl. Phys. Lett.* **2018**, 113, 121114.

[37] Amanti, M. I.; Scalari, G.; Terazzi, R.; Fischer, M.; Beck, M.; Faist, J.; Rudra, A.; Gallo, P.; Kapon, E. Bound-to-continuum terahertz quantum cascade laser with a single-quantum-well phonon extraction/injection stage. *New J. Phys.* **2009**, 11, 125022.

[38] Bismuto, A.; Bidaux, Y.; Blaser, S.; Terazzi, R.; Gresch, T.; Rochat, M.; Muller, A.; Bonzon, C.; Faist, J. High power and single mode quantum cascade lasers. *Opt. Express* **2016**, 24, 10694.

[39] Sampaolo, A.; Yu, C.; Wei, T.; Zifarelli, A.; Giglio, M.; Patimisco, P.; Zhu, H.; Zhu, H.; He, L.; Wu, H. H_2S quartz-enhanced photoacoustic spectroscopy sensor employing a liquid-nitrogen-cooled THz quantum cascade laser operating in pulsed mode. *Photoacoustics* **2021**, 21, 100219.

[40] Li, L.; Chen, L.; Zhu, J.; Freeman, J.; Dean, P.; Valavanis, A.; Davies, A.; Linfield, E. Terahertz quantum cascade lasers with> 1 W output powers. *Electron. Lett.* **2014**, 50, 309-311.

For Table of Contents Use Only

Manuscript title:" Independent Control of Mode Selection and Power Extraction in Terahertz Semiconductor Lasers";

Names of authors: Kai Wang, Hongzhou Bai, Chenren Yu, Haiqing Zhu, Pingping Chen, Wei Lu, Lianhe Li, A.Giles Davies, Edmund H. Linfield, Hua Li, Juncheng Cao, Chong Chen, Harvey E. Beere, Da-vid A. Ritchie , Li He, Gangyi Xu;

Synopsis: We have proposed a novel architecture for semiconductor lasers, in which an active distributed Bragg reflector and a grating coupler are monolithically integrated into the laser ridge, enabling independent control of mode selection and power extraction. The concept has been successfully implemented onto terahertz quantum cascade lasers. Excellent laser performances have been demonstrated, including robust single-mode emission, high output power and high operating temperature. Our work provides an avenue to realize high power single-mode lasers in different material systems at different wavelengths.